Heat-inducible CAR-T overcomes adverse mechanical tumor microenvironment in a 3D bioprinted glioblastoma model

Min Tang [a,1], Yunjia Qu [b,c,1], Peixiang He [b,c], Emmie Yao [a], Tianze Guo [b,c], Di Yu [d], Nancy Zhang [d], Wisarut Kiratitanaporn [b], Yazhi Sun [a], Longwei Liu [e,**], Yingxiao Wang [e,***], Shaochen Chen [a,b,c,*]

[a] Department of NanoEngineering, University of California San Diego, La Jolla, CA, 92093, USA
[b] Department of Bioengineering, University of California San Diego, La Jolla, CA, 92093, USA
[c] Institute of Engineering in Medicine, University of California San Diego, La Jolla, CA, 92093, USA
[d] Department of Human Biology, University of California San Diego, La Jolla, CA, 92093, USA
[e] Alfred E. Mann Department of Biomedical Engineering, University of Southern California, Los Angeles, CA, 90089, USA

ARTICLE INFO

ABSTRACT

Glioblastoma (GBM) presents a significant therapeutic challenge due to the limited efficacy of existing treatments. Chimeric antigen receptor (CAR) T-cell therapy offers promise, but its potential in solid tumors like GBM is undermined by the physical barrier posed by the extracellular matrix (ECM). To address the inadequacies of traditional 2D cell culture, animal models, and Matrigel-based 3D culture in mimicking the mechanical characteristics of tumor tissues, we employed biomaterials and digital light processing-based 3D bioprinting to fabricate biomimetic tumor models with finely tunable ECM stiffness independent of ECM composition. Our results demonstrated that increased material stiffness markedly impeded CAR-T cell penetration and tumor cell cytotoxicity in GBM models. The 3D bioprinted models enabled us to examine the influence of ECM stiffness on CAR-T cell therapy effectiveness, providing a clinically pertinent evaluation tool for CAR-T cell development in stiff solid tumors. Furthermore, we developed an innovative heat-inducible CAR-T cell therapy, effectively overcoming the challenges posed by the stiff tumor microenvironment.

1. Introduction

Glioblastoma (GBM), accounting for approximately 49 % of primary malignant brain tumors in the United States, continues to pose significant clinical challenges due to the failure of surgery, chemotherapy, and radiation to provide a definitive cure [1,2]. Notably, tumor recurrence and progression are common [3,4]. The development of chimeric antigen receptor (CAR) T-cell therapy has exhibited potential in hematologic malignancies and also suggests promise for GBM treatment [4]. However, its application to solid tumors such as GBM faces hurdles largely due to the immunosuppressive tumor microenvironment (TME) and the physical barrier posed by the extracellular matrix (ECM) [5,6]. A characteristic feature of many solid tumors is the stiffening of the tumor ECM, primarily resulting from the overproduction of matrix components

and crosslinking enzymes and a shift towards more rigid types of collagens [7] [–] [9]. The high ECM density and stiffness can affect the abundance, function, and infiltration of cytotoxic T cells, often leading to their exhaustion [10,11]. This complex interplay among the T cells, the ECM, and the TME potentially reduces the effectiveness of current CAR-T cell therapy in solid tumors, as T cells struggle to navigate through the ECM, limiting their ability to reach and attack cancer cells. Understanding the interplay between the CAR-T cells and tumor ECM within the context of biomimetic matrix stiffness could instruct strategies to enhance CAR-T cell therapy efficacy in solid tumors.

However, current modeling systems are limited in their ability to reliably and accurately reproduce the tumor ECM microenvironment. Traditional two-dimensional (2D) in vitro models lack the complex ECM and thus fall short in accurately reflecting the intricate TME. Most of the

---

CAR-T therapies demonstrating good efficacy in 2D cultured cells failed to eradicate solid tumors. Animal models require considerable resources and could be challenging to control and reproduce clinally-relevant tumor stiffness. Three-dimensional (3D) in vitro models offer a promising tool to study the complex interactions between cells and various extracellular matrix (ECM) materials [12] [–] [14]. However, the widespread use of Matrigel-based organoids, while beneficial for culturing primary tumor cells or stem cells, still presents limitations due to its inability to accurately replicate the tissue-specific ECM composition or stiffness of real solid tumors [15]. Matrigel is inherently soft and lacks the mechanical diversity found in the TME. This discrepancy is critical, as the stiffness of the ECM has been shown to significantly influence tumor cell behavior, including proliferation, migration, and drug response. The mechanical properties of the ECM in solid tumors are often much higher than those provided by Matrigel, leading to potential discrepancies in cell morphology, signaling pathways activation, and overall tumor progression in vitro compared to in vivo situations.

Recent advances in 3D bioprinting technology enables encapsulating cells within biomaterials derived from native ECM, providing well-defined architectures and matrix properties to mimic native tissues [16] [–] [18]. Digital light processing (DLP)-based bioprinting has been successfully utilized to create tissue models and cancer models using ECM-derived materials [19–24], and has demonstrated independent control of biophysical properties and biochemical cues when using ECM-derived materials, making it an optimal choice for examining biophysical influences on GBM development within a biomimetic ECM-based model [25–27]. Previous studies have shown that ECM stiffness can modulate tumor cell gene expression, leading to the representation of different cancer subtypes with variable responses to chemotherapy treatments [27]. However, the potential of DLP-bioprinted tumor tissues for evaluating cell therapies, such as CAR-T cell therapy, within 3D biomimetic tumor models remains largely unexplored.

In this study, we utilized DLP-based 3D bioprinting to generate 3D models that carefully modulate the stiffness to mirror normal brain stiffness and pathological GBM tissue stiffness. Our results showed that GBM-relevant stiffness impeded CAR-T cell penetration and reduced their cytotoxicity within the 3D GBM models. This application of 3D bioprinting to model ECM stiffness provided critical insights into its impact on CAR-T cell behavior, laying the groundwork for the development of more effective therapies. Building on these findings, we developed a novel heat-inducible CAR-T cell therapy that effectively navigated the stiff tumor microenvironment, significantly enhancing T cell infiltration and cytotoxicity against tumor cells. This approach demonstrated the potential of heat-inducible CAR-T cells in treating tumors characterized by increased stiffness, offering a promising avenue for therapeutic advancement. Overall, this study both provided a biomimetic 3D bioprinted solid tumor model for more clinically relevant CAR-T evaluation and introduced a novel CAR-T strategy to overcome limitations in CAR-T cell penetration and tumor cytotoxicity in stiff solid tumors.
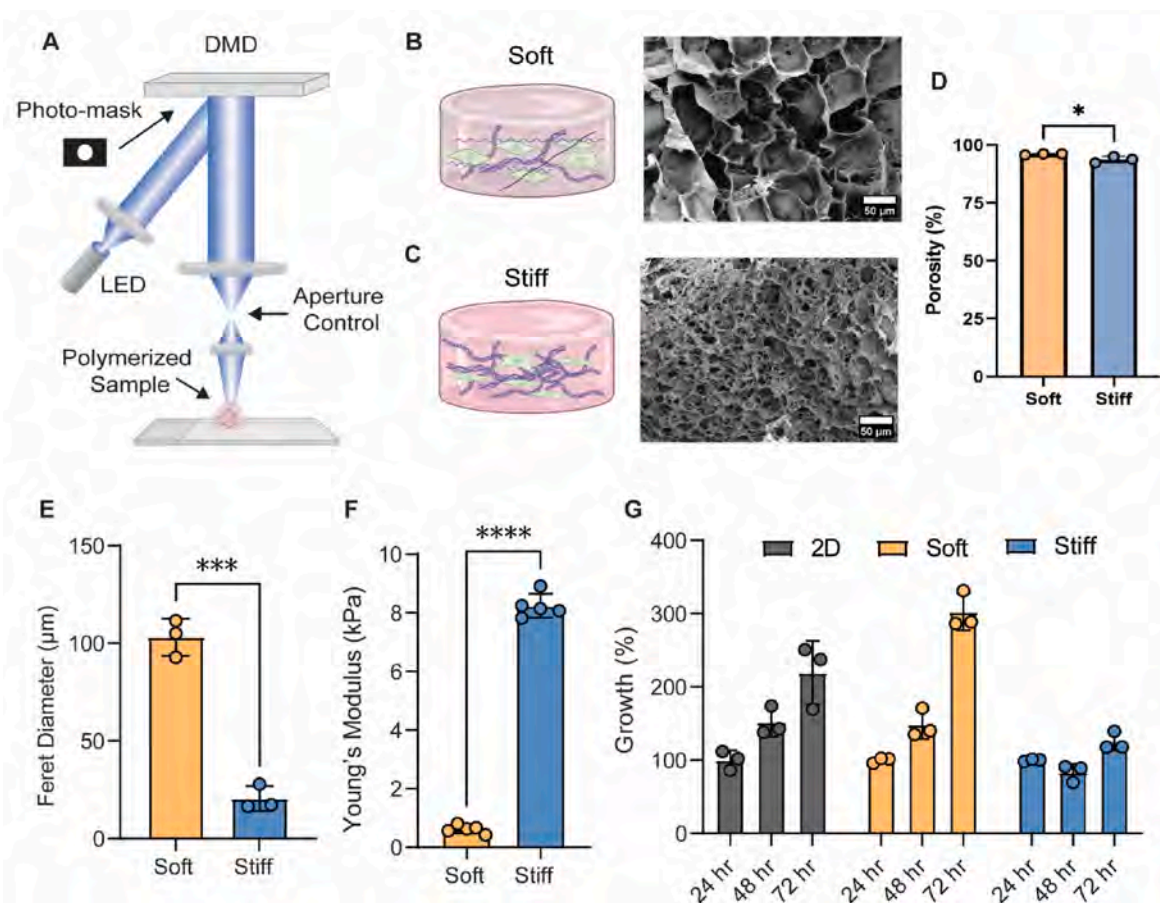

Fig. 1. 3D bioprinted GBM model. (A) A schematic illustration of the DLP bioprinting setup. **(B)** An illustration of the bioprinted soft models encapsulating tumor cells, accompanied by an SEM image of the freeze-dried models. The scale bar represents 50 μm. **(C)** An illustration of the bioprinted stiff models encapsulating tumor cells, with an SEM image of the freeze-dried models. The scale bar represents 50 μm. **(D)** Porosity of the soft and stiff models. **(E)** Quantification of the pore sizes in the soft and stiff models based on SEM images. **(F)** Measurement of the hydrogel stiffness in the soft and stiff models. **(G)** Growth measurement of CW468 cells under sphere culture conditions, 3D soft, and 3D stiff conditions at 24, 48, and 72 h.

2. Results

2.1. Generation of stiffened solid-tumor mimetic tumor model with DLP bioprinting

The ECM composition and properties have been identified as pivotal factors influencing phenotypic expression and genetic alterations within the tumor and stromal cells [28,29]. Our study employed a DLP bioprinting system to generate cylindrical 3D constructs of GBM (Fig. 1A). This system utilized a digital micromirror device (DMD) to accurately project a circular light patterns onto a photosensitive bioink. This bioink comprised of GBM-mimetic biomaterials and GBM cells, which was polymerized layer by layer upon light exposure. The constructs exhibited tunable mechanical properties, achieved through precise adjustment of light exposure and variations in the concentrations of gelatin methacrylate (GelMA) and the photoinitiator, while glycidyl methacrylate hyaluronic acid (GMHA) concentration remains constant to avoid difference caused on cells due to the potential impact of varied hyaluronic acid and subsequent signaling pathways in GBM cells.

Contrary to previous methodologies that incorporated an acellular extracellular matrix (ECM) region with variable stiffness to assess its influence on adjacent tumor cells [27], this study embedded tumor cells within hydrogels of modulated stiffness, more faithfully mimicking the heterogeneity in stiffness observed in actual GBM tissue. The selected stiffness ranges were designed to reflect both normal physiological and GBM-specific pathological states [27,30]. Scanning electron microscopy (SEM) (Fig. 1B–C) was employed to explore the microstructure of these hydrogels. Hydrogels fabricated with lower stiffness demonstrated higher porosity, with measurements of 96.0 % compared to 93.7 % for stiffer models (Fig. 1D). Additionally, soft models featured larger average pore sizes, approximately 103 μm, in contrast to 21 μm observed in the stiff models (Fig. 1E). The resulting stiffness were 0.6 ± 0.1 kPa and 8.2 ± 0.4 kPa for the soft and stiff conditions, respectively (Fig. 1F). The stiff model effectively replicated the characteristics of stiffened high-grade GBM tissues, which were reported to be around 10 kPa [30]. These biophysical cues, mainly pore size and stiffness, are known to impact tumor cell behavior and drug penetrations [31,32].

Our study utilized two distinct GBM cells to represent heterogeneous phenotypes of GBM: an adherent cell line U87-MG and a patient-derived cells, CW468, suspension-cultured as spheres. High cell viability was observed in both the soft and stiff bioprinted hydrogels for both cell types 72-hr post-printing (Figs. S1A–B). Both cell types exhibited enhanced proliferation in the soft hydrogels compared to the stiff ones, with the disparity in growth rates between the soft and stiff models being most pronounced at the 72-hr post-printing time point (Fig. 1F, Fig. S1C). Moreover, the proliferation rates of CW468 cells within soft hydrogels paralleled those observed in a traditional sphere culture (Fig. 1G). hrGiven the documented role of Rho-associated protein kinase (ROCK) adhesion signaling in modulating cell proliferation within varied 3D microenvironments [33], we hypothesized that the observed differences in proliferation rates could be attributed to this pathway. By supplementing the culture medium with ROCK inhibitor Y-27632, the previously inhibited proliferation rate within the stiff models was restored to a level that was comparable with that observed in the soft models, confirming the hypothesis that the observed differences in growth rates could be attributed to cells responding to different matrix stiffness via ROCK pathway (Figs. S2A–B). We have also adopted RNA Sequencing to investigate the variations in gene expression in tumor cells cultured in soft versus stiff 3D models. The data verified that specific biological pathways, including those related to the ROCK pathway, such as cell-cell adhesion, focal adhesion, and regulation of actin cytoskeleton, were significantly enriched under stiff conditions (Figs. S3A–C).

2.2. Standard CAR-T cells exhibited decreased efficacy in stiff 3D bioprinted models

To test the applicability of 3D bioprinted GBM models in evaluating the therapeutic potential of standard CAR-T cells to be used in clinical settings, we engineered GD2-CAR-T cells with high-affinity anti-GD2 single-chain variable fragment (scFV) (Fig. 2A) [34]. Clinical trials with GD2-CAR-T cells have been conducted in pediatric neuroblastoma patients [35] and yet have the chance to be tested in adults, making an in-vitro model using adult GBM cells with greater value in determining the clinical potential of such therapy as adult GBM tissue also have high GD2 expression [36]. Our GD2-CAR-T cells demonstrated high efficacy against tumor cells in 2D culture and sphere culture, leading to approximately 80 % cell death following a 24-hr treatment period (Fig. S3D).

We then investigated the cytotoxic efficacy of CAR-T cells in the 3D bioprinted models under both soft and stiff conditions (Fig. 2B). Tumor cells were bioprinted as previously described and allowed to incubate overnight prior to the exposure of CAR-T cells. The viability of these tumor cells was subsequently tracked and recorded at 24-hr intervals over a total duration of 72 h. In the 3D models, CAR-T cytotoxicity was significantly diminished relative to the 2D or sphere cultures. The U87 cell line demonstrated less than 10 % cytotoxicity in both soft and stiff 3D models after a 24-hr co-culture with the CAR-T cells. Similarly, the CW468 cell line displayed around 30 % cytotoxicity in the soft model and less than 10 % in the stiff model. At the 72-hr mark, the CAR-T cytotoxicity increased to roughly 40 % in the soft models for both cell lines. However, cytotoxicity in the stiff models remained considerably lower than in the soft models (Fig. 2C). This CAR-T efficacy in stiff 3D bioprinted models aligned with the existing challenges of CAR-T therapy efficacy in solid tumors which possess stiffer TME [37].

Immunofluorescent staining at the 72-hr time point was performed to visualize CAR-T cell penetration into the tumor models and the associated tumor cell apoptosis (Fig. 2D–E). One notable observation was the significantly reduced DAPI nuclei staining in soft models, indicating a decreased cell density which could be attributed to greater cell death due to CAR-T cell killing in the soft models. In such cases, tumor cells that died early due to superior CAR-T cell cytotoxicity would have decomposed by the 72-hr mark, leading to undetectable fluorescent signals. In addition, we found fewer infiltrated T cells in the stiff microenvironment, as represented by CD3 staining, potentially leading to the diminished killing of tumor cells (Fig. 2D–E). These results suggested that stiffer microenvironments may limit the effectiveness of current standard CAR-T cells, potentially by hindering T cell penetration into the solid tumors.

2.3. Heating reduced hypoxia and angiogenic status of the tumor cells in the stiff GBM model

With our established 3D GBM model mimicking solid tumors exhibiting resistance to standard GD2-CAR-T treatments, we explored ways to enhance the therapeutic effect of CAR-T. We hypothesized that heat shock (HS) and heat-inducible CAR-T cells might offer better therapeutic effects due to a combined influence of heat on the tumor microenvironment and stimulation of T-cell traffic. The rising temperature in tissue, such as fever, has been shown to enhance immune surveillance via promoting T cell trafficking [38,39], stimulating antigen-specific T cell responses [40], and augmenting cytotoxic T cell metabolism [41]. We aimed to mimic this physiological response by exposing the tumor tissue to slightly higher temperatures (43 °C) in a short duration (<15min), which is significantly above the fever range of 38 °C, to gain full control of our heat-inducible system without causing damage to the tissues [42].

We first compared gene expressions of CW468 cells in the 3D stiff model, with and without heat treatment, using RNA sequencing. The heat treatment (43 °C for 15 min) was applied at the 24-hr and 48-hr
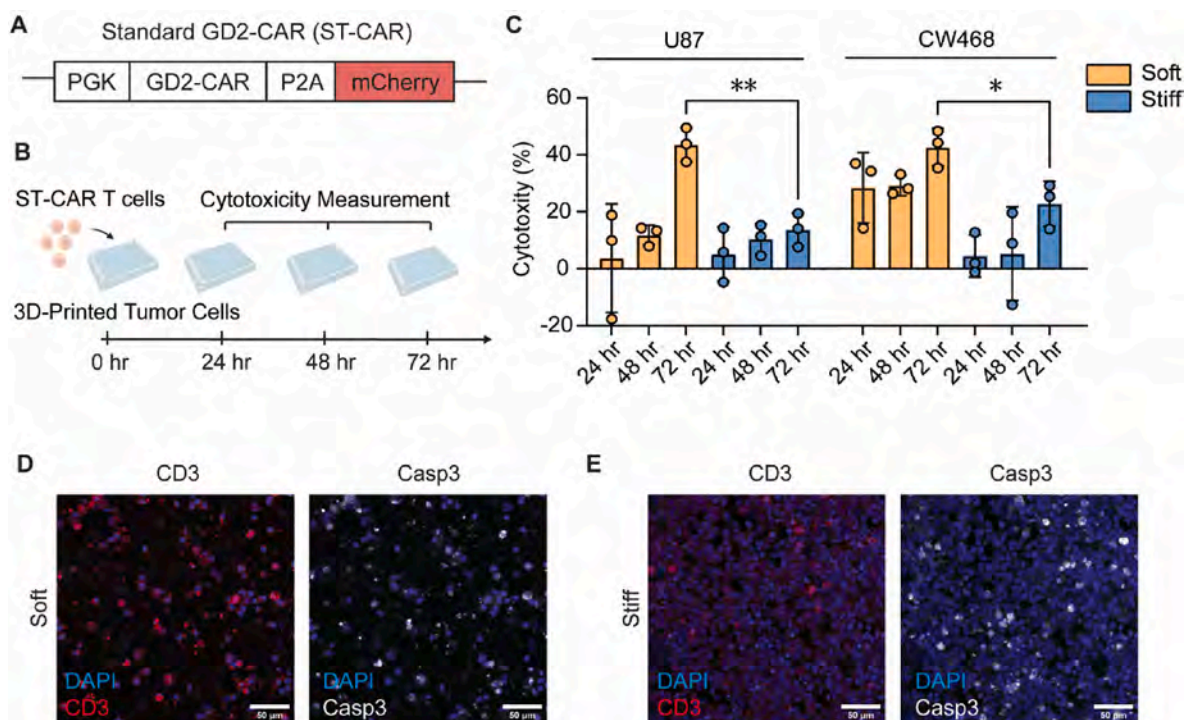
Fig. 2. GD2-CAR-T evaluation in 3D bioprinted model. (**A**) A schematic of the standard GD2-CAR construct. (**B**) A schematic showing CAR-T cell treatment and the measurement of cytotoxicity in 3D co-culture experiments. Standard CAR-T cells were co-cultured with Fluc-expressing U87 or CW468 cells at an E:T ratio of 1:1 in 3D soft and stiff models. Cytotoxicity measurement took place at 24 h, 48 h, and 72 h post T cell treatment. (**C**) Quantification of CAR-T cell-induced cytotoxicity in U87 and CW468 cells within soft and stiff models. (**D, E**) Immunofluorescence staining and confocal imaging were performed on 72-hr soft and stiff samples. Cell nuclei were counterstained with DAPI (blue), penetrated T cells were stained with a CD3 antibody (red), and cells undergoing apoptosis were stained with a Caspase-3 antibody (white). (For interpretation of the references to colour in this figure legend, the reader is referred to the Web version of this article.)

marks, and cells were harvested at the 72-hr mark for RNA extraction and sequencing. Transcriptome profiling revealed differences in CW468 expression cultured in 3D stiff models with and without heating (Fig. 3A), and a Gene Set Enrichment Analysis (GSEA) showed a decrease in mechanistic target of rapamycin (mTOR) complex 1 (mTORC1) signaling and hypoxia in heated CW468 cells (Fig. 3B). Both pathways have been associated with GBM invasion [43], with hypoxia as a GBM hallmark that triggers angiogenesis-related molecules, contributing to immune escape, and the mTORC1 signaling pathways also associated with cellular adaptation to hypoxic tumor microenvironments. To analyze our results further, we performed a Gene Ontology (GO) biological pathway analysis and a KEGG pathway analysis with the differentially expressed genes (DEGs) identified from the RNA sequencing. This analysis confirmed the GSEA results that both hypoxia- and angiogenesis-related pathways were enriched in the non-heated stiff groups (Fig. 3C). Among the top DEGs, GBM-related protein-coding genes like NDUFA4L2, ANGPTL4, LOXL2, NPTX1, L1CAM, and SLC27A3 were upregulated in the non-heated stiff group (Fig. 3D), indicating their potential role in GBM progression, metastasis, and poor prognosis. A hypoxia-inducible long-non-coding RNA, MIR210HG, is known to contribute to GBM malignancy, as well as other tumor progression-related genes, including SLC6A6, ANGPTL4, CA9, SLC18A3, and ZFHX3, were also upregulated (Fig. 3D).

The majority of the genes associated with enriched pathways identified from RNA sequencing analysis were down-regulated in the heated stiff group (Fig. 3E). This supports our premise that heating can mitigate tumor progression pathways, suggesting a mechanistic basis for enhanced tumor-killing capacity by heat-inducible CAR-T cells. However, we observed that the fold changes were relatively small, and no significant pathways were identified in the heated group using upregulated DEGs. This could be due to the heterogeneous nature of patient-derived cells CW468 and the brief and transient heating scheme applied.

Nonetheless, our findings provide valuable insights into the tumor's response to heat, which promotes T-cell migration and is informative for future therapeutic designs.

2.4. Heat-inducible GD2-CAR expression and its functionality in primary human T cells in 2D tumor culture

Recurrent antigen-CAR stimulation can diminish the overall therapeutic efficacy of CAR-T therapies [5,44]. We hypothesized that genetically engineered T cells with controllable and reversible GD2-CAR expression, achieved by appending GD2-CAR to a 7-heat shock element-promoter (7HE) [45] that can be activated by heat (Fig. 4A–B) could offer a transient rest period for CAR-T cells, enhancing overall therapeutic outcomes as previously reported [46]. We first tested the inducibility and reversibility of the designed CAR gene cassette in primary human T cells using a 15 min, 43 °C HS pattern (Fig. 4C). At 6 h post-HS, antibody staining revealed approximately 80 % of cells expressed CAR, which decreased to 30 % at 24 h post-induction. In the absence of heat, no CAR expression was detected, illustrating the low leakage and high inducibility of our system (Fig. 4D–E). Our HS-CAR-T cells can be repetitively induced where a second and third HS with the same heating parameters can successfully induce the T cells to have CAR-expression again (Figs. S4A–B). T cell growth and viability are not affected by the repetitive heating (Figs. S4C–D), however, repetitive heating has shown an effect to further activated T cells through CD69 expression, and grant CAR-T cells with cytotoxicity function with higher Granzyme B and Perforin expressions (Fig. S4E). After co-culturing with antigen-presenting U87 cells, CAR-T cells are further activated and demonstrated much higher cytotoxicity functions (Fig. S4E).

The heat-inducible GD2-CAR-T cells (HS-CAR) were heated using the same HS scheme and then co-cultured with Firefly luciferase (Fluc)-expressing U87 GBM cells in a standard 96-well cell culture plate. The
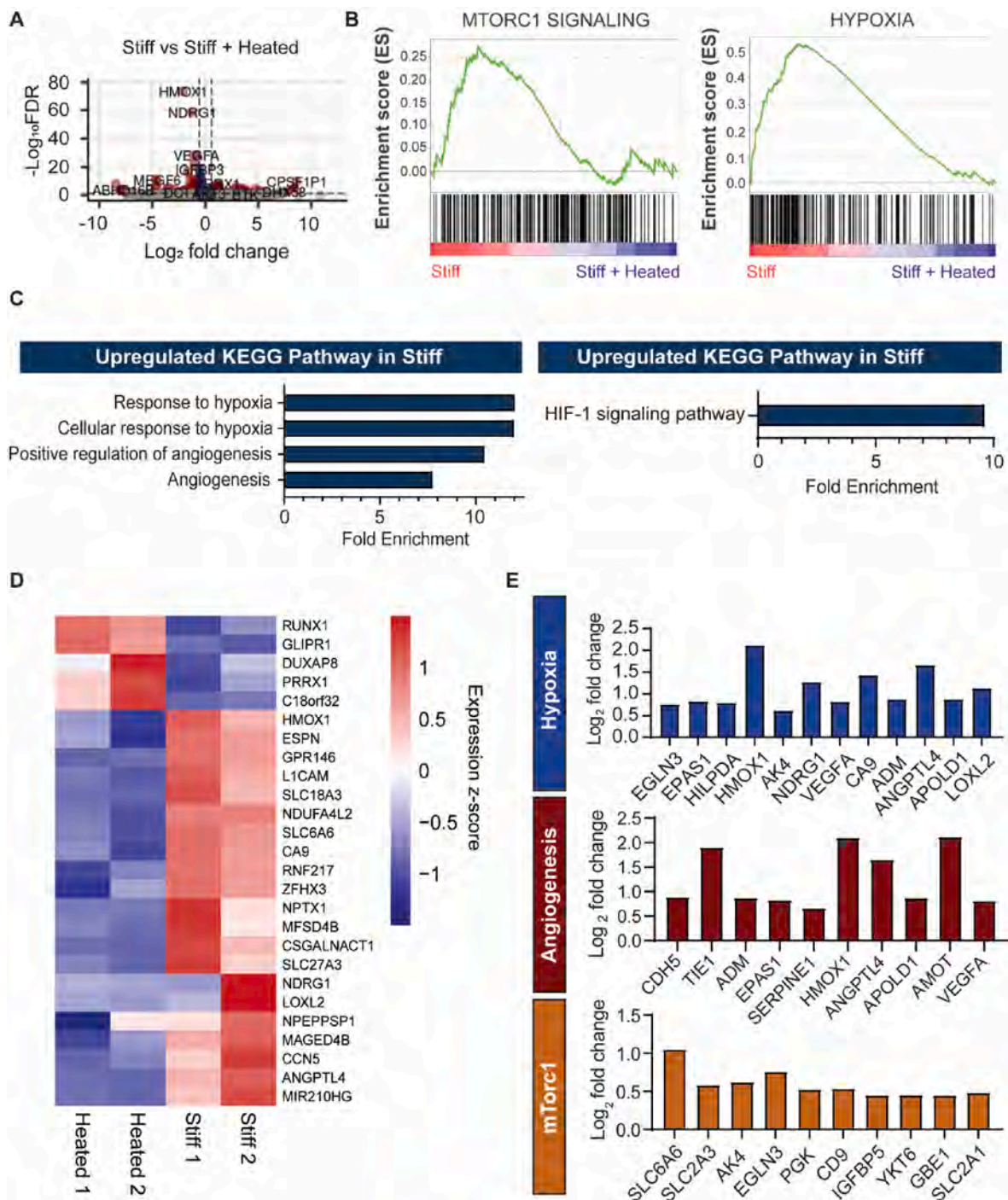
Fig. 3. Distinct transcription profiles in 3D stiff model with and without heating. (**A**) Volcano plot of transcriptional landscape comparing CW468 in 3D stiff model without heating vs. CW468 in 3D stiff model with heating at 24 h and 48 h after printing. The x-axis shows the log2 transformed fold change, and the y-axis shows the negative log-transformed adjusted p-value. n = 2 replicates per condition. (**B**) GSEA analysis of pathways enrichment comparing CW468 grown in the 3D stiff model with (Blue) and without (Red) heating. Nominal P-value <0.05. mTorc1 signaling pathway: NES = 1.47, Hypoxia: NES = 1.43. (**C**) Gene ontology (GO) biological pathway terms (Left) and KEGG pathway terms (Right) enriched in CW468 in 3D stiff culture without heating. DEGs were selected using adjusted $P < 0.05$ and absolute log2FC > 0.58. (**D**) Heatmap of mRNA expression of top differentially expressed genes in CW468 in 3D stiff culture with and without heating. Cells were collected after 72 h of culture in the 3D stiff structure with and without heating. Adjusted $P < 0.05$. The scale bar represents a normalized z-score. (**E**) log2 transformed fold change of representative genes related to hypoxia, angiogenesis, and mTorc1 signaling in CW468 in the 3D stiff model without heating vs. CW468 in the 3D stiff model with heating. Positive log2 transformed fold change values show higher expression in CW468 in 3D stiff culture without heating. (For interpretation of the references to colour in this figure legend, the reader is referred to the Web version of this article.)

engineered T-cell cytotoxicity was assessed at varying effector-to-target (E:T) ratios. After a 24-hr 2D co-culture, the remaining tumor cells were lysed, and luminescence was measured using a plate reader. Increased E:T ratios corresponded to enhanced T cell-mediated killing. The most significant difference between heat-inducible GD2-CAR-T and primary human T cell cytotoxicity was observed at a 1:1 E:T ratio, which eliminated 70 % and 0 % of tumor cells, respectively (Fig. 4F). This E:T ratio was subsequently used in all following 2D and 3D co-culture
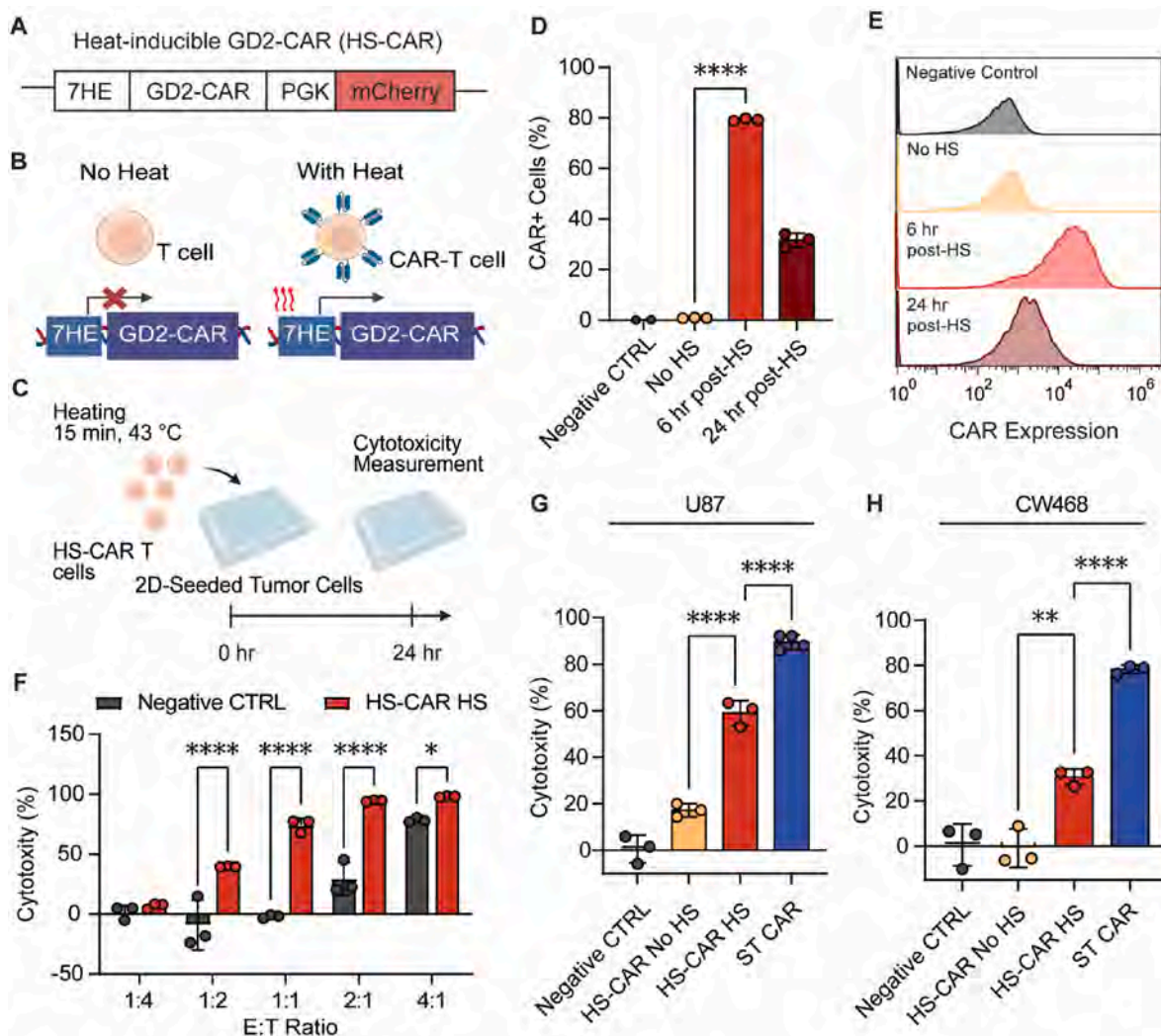
Fig. 4. Development of HS-GD2-CAR-T cell. (**A**) Schematics of HS-GD2-CAR. (**B**) Design of the HS-GD2-CAR-Therapy technology. (**C**) HS and co-culture scheme of the 2D cytotoxicity assays. (**D, E**) CAR induction in primary T cells with HS of 15 min, 43 °C at t = 0 h. CAR expression is measured with anti-mouse-F(ab')2 antibodies staining using flow cytometry. Negative CTRL is plain human primary T cells. (**F**) HS-CAR-T cells (after HS) and Negative CTRL cells were co-cultured with Fluc-expressing U87 cells for 24 h. (**G, H**) HS-CAR (with and without HS), Negative CTRL and standard CAR (ST-CAR) were co-cultured with Fluc-expressing U87 (**G**) or CW468 (**H**) cells at E:T of 1:1 for 24 h. Cytotoxicity percentage was calculated using the luminescence reading from three biological replicates of co-culture wells divided by the readings of three biological replicates with no T cells added. Statistical differences were analyzed using Two-way ANOVA.

experiments.

We also compared the cytotoxicity of our heat-inducible GD2-CAR-T cells and the standard GD2-CAR-T when co-cultured with U87 or CW468 in 2D with 1:1 E:T ratio. Although HS induced a significantly enhanced killing of both tumor cell types by HS-CAR, standard CAR-T cells showed higher cytotoxicity (Fig. 4G–H). The above results demonstrated that the HS-responsive GD2-CAR can efficiently kill tumor cells. However, as expected, with only one round of HS, the killing efficacy of the HS CAR was weaker than that of the constitutive CAR when cultured in a 2D environment, which can be further tuned by repeated heating.

2.5. Heat-inducible CAR-T cells overcome adverse mechanical tumor microenvironments

Finally, we investigated the therapeutic effects of HS-responsive CAR-T cells in the bioprinted models with different mechanical environments. We implemented a regimen of repeated heating (initial heating at 0 h, subsequent heating at 24 and 48 h) with the initial heating applied solely to HS-CAR-T cells and the subsequent heat shocks applied to co-culture plates containing both HS-CAR-T cells and tumor cells. Cytotoxicity was assessed at 24-, 48-, and 72-hr post-co-culture (Fig. 5A).

The implemented heating protocol resulted in no significant alteration in the structure or pore sizes of the stiff hydrogel (Fig. 5B–C). Stiffness and porosity measurements for both stiff and soft models further confirmed that repetitive heating induced no significant changes (Figs. S5A–B). Despite the lack of significant alterations in mechanical properties, enhanced cytotoxicity was observed in HS-CAR-T cells in both models following heating. This increased tumor eliminating efficacy may be attributed to heat-induced alterations in tumor cells and improvements in T cell trafficking or penetration into the ECM.

After 72 h of co-culture with 3D tumor models under repeated heating, HS-CAR-T cells demonstrated significantly higher tumor elimination than standard CAR-T cells in the 3D stiff models using both U87 and CW468 cell lines (Fig. 5D, Fig. S6A). This presented a notable contrast to the results from 2D co-cultures, where HS-CAR exhibited lower cytotoxicity compared to standard CAR-T cells. This disparity may be attributed to the shorter duration of the 2D killing experiments and the one-shot HS pattern, while the HS-CAR-T cells, which exhibited reversible CAR expression, induced higher cytotoxicity as the co-culture
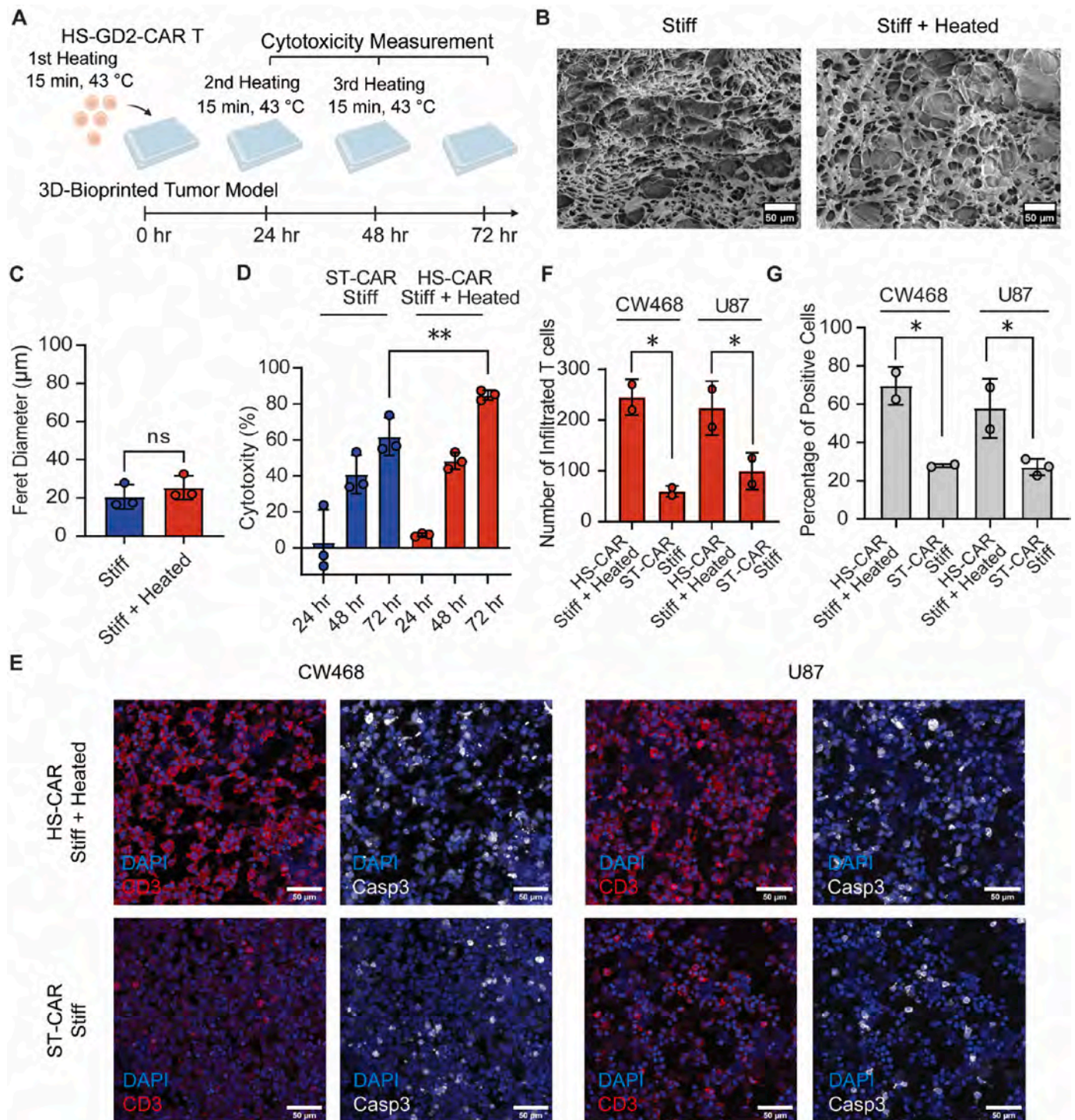
Fig. 5. (**A**) Schematic of heat shocks and cytotoxicity measurement in 3D co-culture experiments. The 1st heating was performed on HS-CAR-T cells only, and 2nd and 3rd heating was performed on HS-CAR-T cells with tumor cells in 3D. ((**B**) SEM images of stiff gel with (Stiff + Heat) or without (Stiff) heating. (**C**) Quantification of pore sizes of Stiff and Stiff + Heated from **B**. (**D-G**) HS-CAR (with HS), and standard CAR (ST-CAR) were co-cultured with Fluc-expressing U87 or CW468 cells at E: T of 1:1 following setup depicted in **a.** in a 3D stiff model. Cytotoxicity measurement was performed 24-, 48-, and 72-hr of ST-CAR with U87 cultured in the stiff model and HS-CAR with U87 cultured in the stiff model with HS (**D**). Immunofluorescence staining and confocal imaging (**E**) were performed on 72 h of stiff samples, and quantification of CD3$^+$ cell number (**F**) and caspase-3+ cells (**G**) was performed using ImageJ. Cell nuclei were stained with DAPI (blue), penetrated T cells were stained with CD3 antibody (Red), and cells undergoing apoptosis were stained with caspase-3 antibody (White). Statistical differences were determined using the two-tailed Student's t-test. (For interpretation of the references to colour in this figure legend, the reader is referred to the Web version of this article.)

duration extended.

We subsequently assessed the cell growth and viability of both U87 and CW468 tumor cells in the heated and non-heated control models. Our findings indicated no significant differences, suggesting that the

applied heating does not directly eradicate tumor cells in our model (Figs. S6B–C). Immunofluorescent staining of CD3$^+$ T cells revealed a much higher population of infiltrating T cells in the 3D stiff model with heating for both cell types (Fig. 5E–F).

Upon examining the z-scan images of infiltrated CAR-T cells with and without repetitive HS stimulation, we observed that HS-CAR-T cells more effectively infiltrated the stiff scaffold, with many T cells reaching up to 100 μm beneath the gel surface (Fig. S6D). Additionally, the heating process appears not to affect T cell adhesion to the extracellular matrix (ECM), as CD29 levels remained unchanged (Figs. S6E–F). Increased caspase-3 staining confirmed that more cells were undergoing apoptosis in the heated 3D stiff models than in non-heated 3D stiff models for both cell types (Fig. 5E–G).

In the 3D soft models, the cytotoxicity and T cell penetration were also enhanced in the HS-CAR-T groups (Fig. 6A–E), but the differences were not as significant as those observed in the 3D stiff models, possibly due to the already high killing efficacies of around 80 % of both U87 and CW468 in the 3D soft models by constitutive GD2-CAR-T cells. In conclusion, our HS-CAR-T cells and the heating scheme have shown higher T cell penetration into the pathology-mimicking 3D stiff

environment, demonstrated higher anti-tumor activities, and overcame standard CAR-T cell therapy resistance in the adverse mechanical microenvironment.

3. Conclusion

Given the challenges associated with creating consistent in vivo GBM models with finely tuned mechanical properties, we employed a DLP bioprinting system to fabricate 3D GBM models with differing matrix stiffness. Our study introduces a novel method for assessing the therapeutic potential of CAR-T cells in solid tumors via physiologically relevant 3D bioprinting, and our findings highlighted that the stiffer models more accurately replicated the pathological conditions associated with brain tumors than their softer counterparts, as demonstrated by significantly reduced pore sizes and potentially quiescent tumor cells. Stiff models also exhibited resistance to standard CAR-T cell therapy, similar
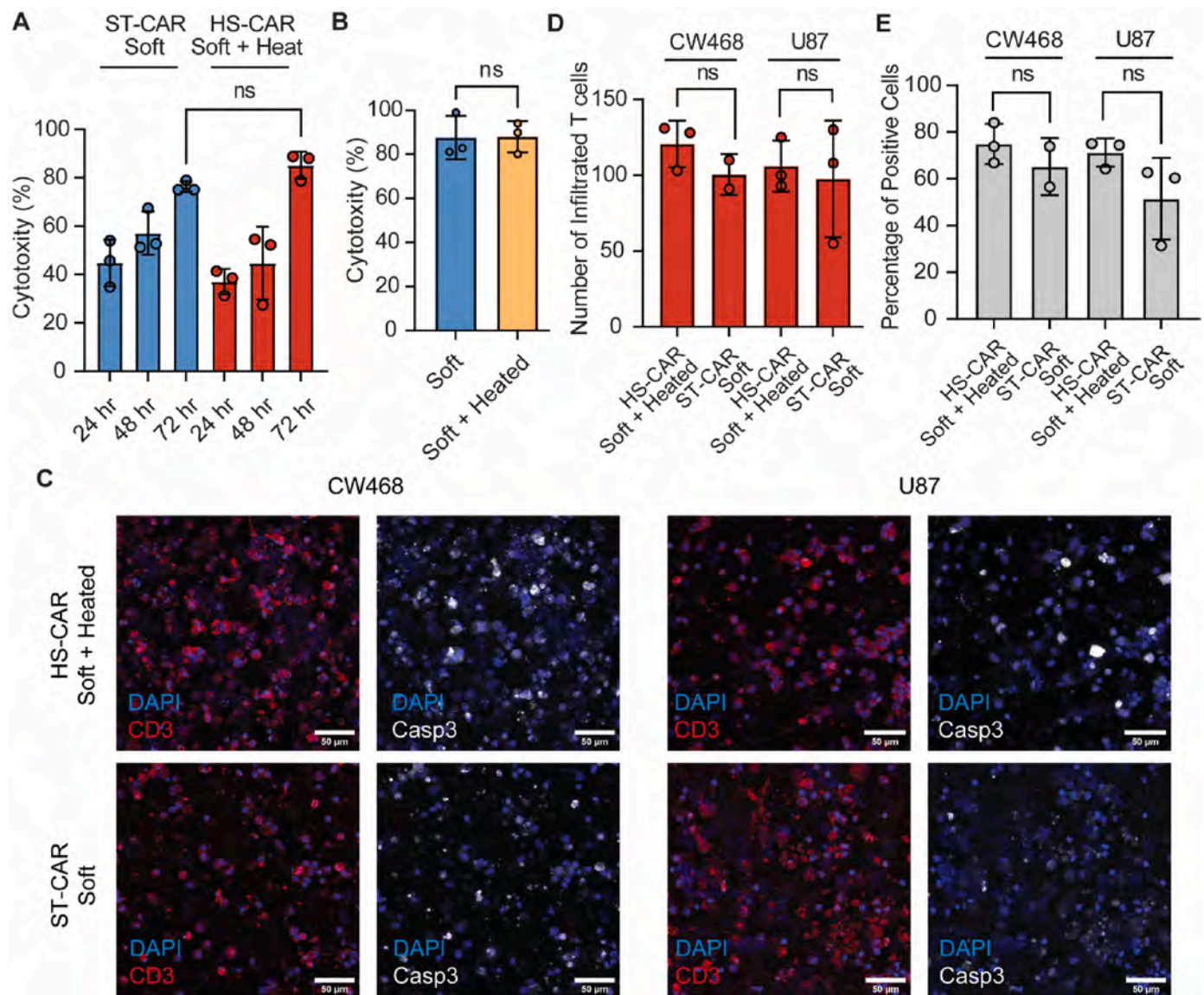

Fig. 6. HS-CAR and ST-CAR were co-cultured with Fluc-expressing U87 or CW468 cells at E:T of 1:1 following the setup depicted in Fig. 4a in the 3D soft model. (**A**) Cytotoxicity measurements were performed at 24-, 48-, and 72-hr intervals for ST-CAR co-cultured with U87 cells and HS-CAR co-cultured with U87 cells in the 3D soft model with HS. (**B**) Cytotoxicity measurements were taken after 72 h for ST-CAR co-cultured with CW468 cells in the 3D soft model, and HS-CAR co-cultured with CW468 cells in the 3D soft model with HS. (**C-E**) Immunofluorescence staining and confocal imaging (**C**) were performed on 72-hr soft samples, and quantification of CD3$^+$ cell numbers (**D**) and the percentage of caspase-3+ cells (**E**) were performed using ImageJ. Cell nuclei were stained with DAPI (blue), T cells were stained with a CD3 antibody (red), and cells undergoing apoptosis were stained with a caspase-3 antibody (white). (For interpretation of the references to colour in this figure legend, the reader is referred to the Web version of this article.)

to that observed in real solid tumors, indicated by diminished cytotoxic effects compared to both 2D cultures and softer models. This resistance could be attributed to reduced T-cell penetration and the enrichment of specific gene expression pathways under stiffer conditions.

Despite CAR-T cells' potential as transformative cancer therapies, their risk of "on-target, off-tumor" toxicity remains a significant concern, potentially harming non-malignant tissues [47,48]. To address this, various strategies for remotely controlling CAR-T cell activation have been explored, such as heat shock and ultrasound-induced activation, to mitigate risks and enhance safety [42,49]. To combat the insufficient tumor eradication observed with standard GD2-CAR-T cells in stiff tumors, we thus incorporated a strategy involving genetically modified T-cells to allow for controllable and reversible GD2-CAR expression via a heat-inducible promoter.

We demonstrated that heating significantly reduced hypoxia and mTORC1 signaling in tumor cells in our 3D bioprinted stiff models. The genes involved in these pathways have been associated with GBM progression, increased metastasis, and poor prognosis. Next, with the design of heat-shock promoter-driven GD2-CAR-T cells in 2D experiments, our HS-GD2-CAR has demonstrated the significant killing difference of GBMs employed with and without HS due to GD2-CAR induction difference upon heat shock. Remarkably, these cells displayed significantly enhanced tumor ECM penetrating capability and tumor cell killing in 3D environments following HS induction, especially in stiff conditions mimicking solid tumors. This result suggests the potential that our HS-CAR-T cells will benefit from long-term efficacy as its nature renders antigen-CAR interaction for a controlled time frame, allowing minimal T cells exhaustion and optimal therapeutic efficacy in the future. When these heat-inducible CAR-T cells were applied to our 3D bioprinted models, repeated heating led to a substantially higher tumor eradication level than standard CAR-T cells, particularly in the stiffer models. This enhancement was not due to direct cell killing by heat but instead resulted from increased T-cell penetration into the extracellular matrix. These results indicate that heat-inducible CAR-T cells, coupled with heating, can mitigate the solid tumor-like conditions of stiff models, enhance T cell penetration, and suppress tumor-promoting gene expression pathways, thereby boosting the efficacy of CAR-T cell therapy in GBMs.

In this study, we have focused primarily on ECM stiffness, a critical feature of solid tumor. Future iterations could integrate additional tumor microenvironment aspects, such as immune cell infiltration, inflammation, and other ECM components, to refine our model. Nevertheless, our 3D bioprinting approach successfully recapitulates the challenges of CAR-T cell infiltration and efficacy in solid tumors and inspired the development of HS-CAR-T. This demonstrates the potential of our biomimetic model as a platform for evaluating and optimizing solid tumor-targeting CAR-T cell therapies in a physiologically relevant setting.

4. Materials and methods

4.1. Bioink preparation

GelMA was synthesized using Type A, gel strength 300 gelatin derived from porcine skin (Sigma Aldrich cat #: G2500). Briefly, a 10 % (w/v) solution of gelatin was prepared by dissolving gelatin in a 3:7 carbonate-bicarbonate buffer solution (pH ~9) at 50 °C. To achieve a 95 % degree of methacrylatetion, methacrylic anhydride was gradually added at a rate of 0.1 mL/(g of gelatin). This reaction proceeded for an hour at 50 °C. Following synthesis, the solutions were dialyzed at 42 °C for up to a week, frozen at −80 °C overnight, and lyophilized for up to 72 h. The degree of methacrylatetion was measured using proton NMR (Bruker, 600 MHz). GMHA was synthesized using 200 kDa hyaluronic acid (HA, Lifecare Biomedicals). HA was dissolved in deionized water at a concentration of 1 % overnight with stirring. On the next day, triethylamine and glycidyl methacrylate were sequentially added to the

mixture dropwise and stirred overnight in the dark. GMHA was then precipitated with 4 L/(g of HA) of acetone and redissolved in deionized water at a concentration of 1 %. The resuspended GMHA solution was dialyzed at room temperature for 12 h, frozen at −80 °C overnight, and lyophilized for up to 72 h. The lyophilized GelMA and GMHA were then stored at −80 °C and reconstituted to a stock solution of 20 % (w/v) and 4 % (w/v) before printing. Both solutions were subjected to sterilization using 0.22 μm filters before mixing with cells (Millipore). Lithium phenyl-2,4,6-trimethylbenzoylphosphinate (LAP, TCI Chemical) was dissolved in DPBS to a stock solution of 4 % (w/v) and stored at 4 °C.

4.2. Cell culture

Human GBM U87 cells were cultured in Dulbecco's Modified Eagle Medium (DMEM) (Gibco, 11995115) supplemented with 10 % fetal bovine serum (FBS) (Gibco, 10438026) and 1 % penicillin–streptomycin (P/S) (Gibco, 15140122). Primary human T cells were cultured in X–VIVO 15 (LONZA, 04-418Q) supplemented with 5 % FBS, 1 % P/S, 50 μM 2-Mercaptoethanol (Gibco, 31350010), and 100 U/ml recombinant human IL-2 (PeproTech, 200-02). Patient-derived GBM CW468 cells gifted by Dr. Jeremy Rich Lab were cultured in suspension-culture flasks with Neurobasal medium supplemented with 1x B27 minus Vitamin A, 1x Glutamax, 1x sodium pyruvate, 1x P/S, 10 ng/mL basic human fibroblast growth factor (bFGF), and 10 ng/mL human epidermal growth factor (EGF). CW468 cells were passaged using Accutase (Stemcell Technology).

4.3. Bioprinting of tumor models

For cellular printing, tumor cells were digested with TrypLE (U87 cells) or Accutase (CW468 cells). For all 3D samples, the tumor cells were resuspended to a cell density of 4×10^7 cells/mL. Prepolymer printing solution was prepared by diluting the stock solution of GelMA, GMHA, and LAP in DPBS to a final concentration of 10 %, 0.2 %, and 0.3 % for the soft condition, and 15 %, 0.2 %, and 0.6 % for the stiff condition. The cell suspension and prepolymer printing solution were mixed at a 1:1 ratio immediately before printing. The cellular-prepolymer solution was loaded onto a glass slide with PDMS spacers to control the thickness of the samples. The light intensity of the bioprinting setup was adjusted accordingly for the soft and the stiff models, at 11 mW/cm^2 and 24 mW/cm^2, respectively. For each sample, 5 μL of cellular-prepolymer solution was used, resulting in a final cell number of 1×10^5 cells/sample. The thickness of the sample was printed as 500 μm. Printed constructs were rinsed with DPBS and cultured in the cell culture medium at 37 °C.

4.4. Mechanical testing

The prepolymer solution was prepared as described. Pillar structures with 500 μm thickness and a diameter of 500 μm were printed. The printed samples were incubated overnight. The compressive modulus of the samples was then measured using MicroTester (CellScale). Briefly, stainless steel beams and platens were assembled and used to compress the bioprinted samples at 50 μm three times. The final compressing data was used for analysis. Customized MATLAB scripts were utilized to derive the compressive modulus from the force and displacement data.

The porosity of the hydrogels was measured using the following protocol. First, the hydrogels were fabricated and subsequently incubated in PBS. The incubation process varied depending on the experimental group: samples in the non-heated group were soaked in PBS without additional treatment, while samples in the heated group were subjected to heating cycles at 24-h intervals for a total of three sessions. After incubation, all hydrogels were freeze-dried for 72 h. The dry weight of the samples W_d was recorded. Subsequently, these dried samples were immersed in ethanol overnight to ensure complete saturation. The weight of the ethanol-saturated samples W_s was then

determined. The porosity of each hydrogel sample was calculated using the equation:

$$Porosity = \frac{(W_s - W_d)}{\rho V} \times 100\% \qquad (1)$$

4.5. Cloning

Plasmids used in this work are cloned using Gibson Assembly (NEB, E2611L). PCR was performed using Q5 DNA polymerase (NEB, M0491) and synthesized primers (Integrated DNA Technologies). Constructed plasmid sequences were verified by Sanger sequencing (Genewiz).

4.6. Human primary T cell isolation, transduction, and cell sorting

Human peripheral blood mononuclear cells (PBMC) were isolated from buffy coats (San Diego Blood Bank) using a lymphocyte separation medium (Corning, 25-072-CV). Primary human T cells were further isolated from PBMC using the Pan T Cell Isolation Kit (Miltenyi, 130-096-535). Isolated primary human T cells were activated with Dynabeads Human T-Expander CD3/CD28 (Gibco, 11141D) at 1:1 cells-to-beads ratio. T cell spiculations were conducted 48 h after Dyna beads activation, in which activated T cells with lentivirus at the multiplicity of infection (MOI) = 10 were mixed and put into well plates pre-coated with Retronectin (Takara, T100B), followed by centrifugation at 1800g 32 °C for 1 h. Following the three-day culture, fluorescence-activated cell sorting (FACS) was performed with SONY SH800S Cell Sorter.

4.7. Staining, flow cytometry, and quantification of CAR expression in primary human T cells

Staining of cell surface CAR expression for flow cytometry was performed using Alexa Fluor® 647 AffiniPure F(ab')₂ Fragment Goat Anti-Mouse IgG (H + L) (Jackson ImmunoResearch Laboratories Inc. 115-606-062) following manufacture protocols. Staining of surface marker CD69 expression was performed using APC anti-human CD69 Antibody (BioLegend), and intracellular staining of Granzyme B and perforin expression were performed using Alexa Fluor® 647 anti-human/mouse Granzyme B Antibody and Alexa Fluor® 488 anti-human Perforin Antibody (BioLegend) for flow cytometry measurments. Cells were washed and stained using 1:100 antibody dilution in 100 µl PBS, incubated in the dark at room temperature for 30 min, and washed three times before flow cytometry analysis (BD Accuri C6). Gating was based on non-engineered cells with the same staining. Flow cytometry data were analyzed using FlowJo software (FlowJo).

4.8. 2D co-culture and heat shock

For Fig. 3c heating, a thermos cycler (Bio-Rad, 1851148) was used to heat the HS-CAR-T cells at a concentration of 0.5–1 million cells per 50 µl per PCR tube at 43 °C for 15 min. Heated cells were returned to co-culture with indicated E:T ratios with U87 or CW468 under standard conditions.

4.9. 3D co-culture and heat shock

For the first heating in Fig. 4a, a thermos cycler (Bio-Rad, 1851148) was used to heat the HS-CAR-T cells at a concentration of 0.5–1 million cells per 50 µl per PCR tube at 43 °C for 15 min. Heated cells were returned to co-culture with 1:1 E:T ratio with U87 or CW468 cultured in 3D bioprinted models. For the second and third heating in Fig. 4a, plates containing co-cultured models with T cells were heated using a water bath at 43 °C for 15 min. Heated co-cultures were returned to standard cell culture conditions after each heating.

4.10. 2D and 3D cell proliferation and viability measurement

Fluc + U87 cells or Fluc + CW468 cells were cultured with indicated conditions and duration. E:T ratio was calculated by the seeding number of tumor cells and added on the same day after printing or cell seeding to account for the growth. Cells were lysed and luciferase readings were collected to assess cell proliferation. For 2D cultures: in the U87 cell co-culture, the media were aspirated and replaced with 200 µL of 1X cell lysis buffer (Promega, E1531), and in the CW468 cell co-culture, the media were retained, and 100 µL of 2X cell lysis buffer were added. The samples were then incubated at room temperature for 15 min. For 3D cultures, the hydrogel was washed once using PBS and dissolved using collagenase (Sigma, C6885, 1500U/ml in HBSS) for 15 min under 37 °C, and cells were pelleted subsequently. Pelleted cells were resuspended using 1X cell lysis buffer. The luminescence of each specimen was then assessed using the One-Glo Luciferase Assay System (Promega, E6110), adhering to the manufacturer's guidelines. The growth percentage of the sample was determined by percentage change from 24-hr reference. T cell growth with and without HS were monitored using Nexcelom Cellometer K2 Cell Counter at 0 h, 24 h, 48 h, and 72 h.

Cell viability was measured using the LIVE/DEAD™ Cell Imaging Kit (488/570) and a confocal microscope (Leica). Live or dead cell number was counted using ImageJ. Viability was calculated by dividing live cells counted over live plus dead cells counted. T cell viability with and without HS was measured using AOPI with Nexcelom Cellometer K2 Cell Counter at 24 h, 48 h, and 72 h.

4.11. 2D and 3D cytotoxicity measurement

Fluc + U87 cells or CW468 cells grown on 2D or 3D bioprinted models were seeded with engineered primary human T cells following indicated heat shock and E:T ratios; control groups without T cells were included. The mixtures were subsequently grown in standard culture conditions. For 2D cytotoxicity measurement: in the U87 cell co-culture, the media were aspirated and replaced with 200 µL of 1X cell lysis buffer (Promega, E1531), and in the CW468 cell co-culture, the media were retained, and 100 µL of 2X cell lysis buffer were added. The samples were then incubated at room temperature for 15 min. For 3D cytotoxicity measurement, the hydrogel was washed once using PBS and dissolved using collagenase (Sigma, C6885, 1500U/ml in HBSS) for 15 min under 37 °C, and cells were pelleted subsequently. Pelleted cells were resuspended using 1X cell lysis buffer. The luminescence of each specimen was then assessed using the One-Glo Luciferase Assay System (Promega, E6110), adhering to the manufacturer's guidelines. The cytotoxicity percentage of the sample was determined by formula (1 – luminescence of killing group/luminescence of control group) multiplied by 100 %.

4.12. SEM

Bioprinted samples were incubated overnight and snap-frozen in liquid nitrogen. The frozen samples were lyophilized for 24 h. Before SEM imaging, the freeze-dried samples were coated with iridium using a sputter coater (Emitech). Microscopic patterns of the bioprinted structures were then observed and captured using a scanning electron microscope (Zeiss).

4.13. Immunofluorescent staining and confocal imaging

Bioprinted samples (both soft and stiff) co-cultured with standard CAR-T or HS-CAR-T cells were rinsed with DPBS three times and fixed with 4 % paraformaldehyde for 1 h at room temperature. The block/permeabilization solution consisted of 5 % bovine serum albumin (BSA, Gemini Bio-Products) and 0.1 % Triton X-100 (Promega) in DPBS. The fixed samples were blocked/permeabilized for an hr at room temperature. The primary antibodies, including CD3 (Invitrogen), CD29

(Invitrogen), and Caspase-3 (Cell Signaling Technology), were diluted at a ratio of 1:100 in the staining buffer (BioLegend). The samples were incubated in this primary antibody mixture overnight at 4 °C. Following this, the structures were rinsed three times with DPBS supplemented with 0.05 % Tween 20 (PBST) at room temperature. Secondary Alexa Fluor-conjugated antibodies (1:200; Cell Signaling Technology) and DAPI (1:1000) were diluted in the staining buffer. The samples were then left to incubate in the secondary antibody and counterstain mixtures for 1 h in the dark at room temperature. The structures were rinsed three times again with PBST. After the last rinse, the samples were immersed in a DPBS containing 0.05 % sodium azide (Alfa Aesar). A confocal microscope (Leica) was used for capturing images, with the same settings maintained for each primary antibody. Quantifications of the mean fluorescence intensity are performed using ImageJ. Z-scan images are reconstructed using 3D volume viewer in ImageJ.

4.14. RNA extraction and RNA sequencing

CW468 cells were extracted from the printed structures by digesting the hydrogels using collagenase type II (Sigma-Aldrich). Cell lysates were then prepared by mixing TRIzol reagent (Life Technologies) with the tumor cell pellets. The Direct-zol RNA MicroPrep Kit (Zymo) was used to extract the total RNA from each sample. The RNA concentrations in each sample were then assessed using a Tecan plate reader after resuspending the RNA in RNase-free water. After evaluation, the RNA samples were stored at −80 °C before library preparation and sequencing. For all samples, paired-end FASTQ sequencing reads were produced on Illumina NovaSeq 6000 (Novogene).

For RNA sequencing analysis, to trim and filter low-quality reads, we used Trim Galore (v0.6.5, https://github.com/FelixKrueger/TrimGalore). After quality control using fastqc, each fastq file was mapped to the human hg38 genome with gene annotation from GENCODE version 33, and transcript numbers were quantified using Salmon (https://combine-lab.github.io/salmon/). Differentially expressed gene analysis was performed using the edgeR (version 4.3) package. Significant DEGs were determined by a false discovery rate <0.05 and an absolute value of log2FC greater than 0.58. Gene ontology terms were identified using DAVID Bioinformatics Resources, and gene set enrichment analysis was performed with the GSEA desktop application (http://software.broadinstitute.org/gsea/downloads.jsp) and the molecular signatures database.

4.15. Statistical analysis

Statistical analyses were performed using Prism software (GraphPad). Detailed analysis descriptions were included in corresponding figure captions.

CRediT authorship contribution statement

Min Tang: Writing – review & editing, Writing – original draft, Visualization, Validation, Software, Methodology, Investigation, Formal analysis, Data curation. **Yunjia Qu:** Writing – review & editing, Writing – original draft, Visualization, Validation, Software, Methodology, Investigation, Formal analysis, Data curation, Conceptualization. **Peixiang He:** Investigation. **Emmie Yao:** Investigation. **Tianze Guo:** Investigation. **Di Yu:** Investigation. **Nancy Zhang:** Investigation. **Wisarut Kiratitanaporn:** Visualization. **Yazhi Sun:** Visualization. **Longwei Liu:** Writing – review & editing, Writing – original draft,

Project administration, Conceptualization. **Yingxiao Wang:** Writing – review & editing, Writing – original draft, Funding acquisition, Conceptualization. **Shaochen Chen:** Writing – review & editing, Writing – original draft, Funding acquisition, Conceptualization.

Declaration of competing interest

The authors declare that they have no known competing financial interests or personal relationships that could have appeared to influence the work reported in this paper.

Data availability

Data will be made available on request.

Appendix A. Supplementary data

Supplementary data to this article can be found online at https://doi.org/10.1016/j.mtbio.2024.101077.

References

[1] Q.T. Ostrom, M. Price, C. Neff, G. Cioffi, K.A. Waite, C. Kruchko, J.S. Barnholtz-Sloan, CBTRUS statistical report: primary brain and other central nervous system tumors diagnosed in the United States in 2015–2019, Neuro Oncol. 24 (2022) v1–v95, https://doi.org/10.1093/neuonc/noac202.

[2] L.R. Schaff, I.K. Mellinghoff, Glioblastoma and other primary brain malignancies in adults: a review, JAMA 329 (2023) 574–587, https://doi.org/10.1001/jama.2023.0023.

[3] K.K. Das, R. Kumar, Pediatric glioblastoma, in: S. De Vleeschouwer (Ed.), Glioblastoma, Codon Publications, Brisbane (AU), 2017. http://www.ncbi.nlm.nih.gov/books/NBK469983/. (Accessed 30 June 2023).

[4] M. D, D. Py, S. R, L. Gp, P. Ad, J. Ch, CAR T-cell therapies in glioblastoma: a first look, Clin. Cancer Res. : An Official Journal of the American Association for Cancer Research 24 (2018), https://doi.org/10.1158/1078-0432.CCR-17-2871.

[5] L. Liu, Y. Qu, L. Cheng, C.W. Yoon, P. He, A. Monther, T. Guo, S. Chittle, Y. Wang, Engineering chimeric antigen receptor T cells for solid tumour therapy, Clin. Transl. Med. 12 (2022) e1141, https://doi.org/10.1002/ctm2.1141.

[6] L.A.K. Fonkoua, O. Sirpilla, R. Sakemura, E.L. Siegler, S.S. Kenderian, CAR T cell therapy and the tumor microenvironment: current challenges and opportunities, Molecular Therapy - Oncolytics 25 (2022) 69–77, https://doi.org/10.1016/j.omto.2022.03.009.

[7] H. Salmon, K. Franciszkiewicz, D. Damotte, M.-C. Dieu-Nosjean, P. Validire, A. Trautmann, F. Mami-Chouaib, E. Donnadieu, Matrix architecture defines the preferential localization and migration of T cells into the stroma of human lung tumors, J. Clin. Invest. 122 (2012) 899–910, https://doi.org/10.1172/JCI45817.

[8] M. Chirivì, F. Maiullari, M. Milan, D. Presutti, C. Cordiglieri, M. Crosti, M.L. Sarnicola, A. Soluri, M. Volpi, W. Święszkowski, D. Prati, M. Rizzi, M. Costantini, D. Seliktar, C. Parisi, C. Bearzi, R. Rizzi, Tumor extracellular matrix stiffness promptly modulates the phenotype and gene expression of infiltrating T lymphocytes, Int. J. Mol. Sci. 22 (2021) 5862, https://doi.org/10.3390/ijms22115862.

[9] D.E. Kuczek, A.M.H. Larsen, M.-L. Thorseth, M. Carretta, A. Kalvisa, M.S. Siersbæk, A.M.C. Simões, A. Roslind, L.H. Engelholm, E. Noessner, M. Donia, I.M. Svane, P. thor Straten, L. Grøntved, D.H. Madsen, Collagen density regulates the activity of tumor-infiltrating T cells, J Immunother Cancer 7 (2019) 68, https://doi.org/10.1186/s40425-019-0556-6.

[10] H. Salmon, K. Franciszkiewicz, D. Damotte, M.-C. Dieu-Nosjean, P. Validire, A. Trautmann, F. Mami-Chouaib, E. Donnadieu, Matrix architecture defines the preferential localization and migration of T cells into the stroma of human lung tumors, J. Clin. Invest. 122 (2012) 899–910, https://doi.org/10.1172/JCI45817.

[11] D.H. Peng, B.L. Rodriguez, L. Diao, L. Chen, J. Wang, L.A. Byers, Y. Wei, H. A. Chapman, M. Yamauchi, C. Behrens, G. Raso, L.M.S. Soto, E.R.P. Cuentes, I. I. Wistuba, J.M. Kurie, D.L. Gibbons, Collagen promotes anti-PD-1/PD-L1 resistance in cancer through LAIR1-dependent CD8+ T cell exhaustion, Nat. Commun. 11 (2020) 4520, https://doi.org/10.1038/s41467-020-18298-8.

[12] J.P. Woodley, D.W. Lambert, I.O. Asencio, Understanding fibroblast behavior in 3D biomaterials, Tissue Eng., Part B 28 (2022) 569–578, https://doi.org/10.1089/ten. TEB.2021.0010.

[13] M. Liu, C. Wu, L. Ke, Z. Li, Y.-L. Wu, Emerging biomaterials-based strategies for inhibiting vasculature function in cancer therapy, Small Methods 5 (2021) e2100347, https://doi.org/10.1002/smtd.202100347.

[14] D. Caballero, C.M. Abreu, A.C. Lima, N.N. Neves, R.L. Reis, S.C. Kundu, Precision biomaterials in cancer theranostics and modelling, Biomaterials 280 (2022) 121299, https://doi.org/10.1016/j.biomaterials.2021.121299.

[15] E.A. Aisenbrey, W.L. Murphy, Synthetic alternatives to Matrigel, Nat. Rev. Mater. 5 (2020) 539–551, https://doi.org/10.1038/s41578-020-0199-8.

[16] A. Lee, A.R. Hudson, D.J. Shiwarski, J.W. Tashman, T.J. Hinton, S. Yerneni, J. M. Bliley, P.G. Campbell, A.W. Feinberg, 3D bioprinting of collagen to rebuild components of the human heart, Science 365 (2019) 482–487, https://doi.org/10.1126/science.aav9051.

[17] B. Grigoryan, S.J. Paulsen, D.C. Corbett, D.W. Sazer, C.L. Fortin, A.J. Zaita, P. T. Greenfield, N.J. Calafat, J.P. Gounley, A.H. Ta, F. Johansson, A. Randles, J. E. Rosenkrantz, J.D. Louis-Rosenberg, P.A. Galie, K.R. Stevens, J.S. Miller, Multivascular networks and functional intravascular topologies within biocompatible hydrogels, Science 364 (2019) 458–464, https://doi.org/10.1126/science.aav9750.

[18] L. Neufeld, E. Yeini, N. Reisman, Y. Shtilerman, D. Ben-Shushan, S. Pozzi, A. Madi, G. Tiram, A. Eldar-Boock, S. Ferber, R. Grossman, Z. Ram, R. Satchi-Fainaro, Microengineered perfusable 3D-bioprinted glioblastoma model for in vivo mimicry of tumor microenvironment, Sci. Adv. 7 (2021), https://doi.org/10.1126/sciadv. abi9119 eabi9119.

[19] M. Tang, Q. Xie, R.C. Gimple, Z. Zhong, T. Tam, J. Tian, R.L. Kidwell, Q. Wu, B. C. Prager, Z. Qiu, A. Yu, Z. Zhu, P. Mesci, H. Jing, J. Schimelman, P. Wang, D. Lee, M.H. Lorenzini, D. Dixit, L. Zhao, S. Bhargava, T.E. Miller, X. Wan, J. Tang, B. Sun, B.F. Cravatt, A.R. Muotri, S. Chen, J.N. Rich, Three-dimensional bioprinted glioblastoma microenvironments model cellular dependencies and immune interactions, Cell Res. 30 (2020) 833–853, https://doi.org/10.1038/s41422-020-0338-1.

[20] S. You, Y. Xiang, H.H. Hwang, D.B. Berry, W. Kiratitanaporn, J. Guan, E. Yao, M. Tang, Z. Zhong, X. Ma, D. Wangpraseurt, Y. Sun, T. Lu, S. Chen, High cell density and high-resolution 3D bioprinting for fabricating vascularized tissues, Sci. Adv. 9 (2023) eade7923, https://doi.org/10.1126/sciadv.ade7923.

[21] M. Wang, W. Li, J. Hao, A. Gonzales, Z. Zhao, R.S. Flores, X. Kuang, X. Mu, T. Ching, G. Tang, Z. Luo, C.E. Garciamendez-Mijares, J.K. Sahoo, M.F. Wells, G. Niu, P. Agrawal, A. Quiñones-Hinojosa, K. Eggan, Y.S. Zhang, Molecularly cleavable bioinks facilitate high-performance digital light processing-based bioprinting of functional volumetric soft tissues, Nat. Commun. 13 (2022) 3317, https://doi.org/10.1038/s41467-022-31002-2.

[22] F. Zhou, Y. Hong, R. Liang, X. Zhang, Y. Liao, D. Jiang, J. Zhang, Z. Sheng, C. Xie, Z. Peng, X. Zhuang, V. Bunpetch, Y. Zou, W. Huang, Q. Zhang, E.V. Alakpa, S. Zhang, H. Ouyang, Rapid printing of bio-inspired 3D tissue constructs for skin regeneration, Biomaterials 258 (2020) 120287, https://doi.org/10.1016/j.biomaterials.2020.120287.

[23] H.H. Hwang, S. You, X. Ma, L. Kwe, G. Victorine, N. Lawrence, X. Wan, H. Shen, W. Zhu, S. Chen, High throughput direct 3D bioprinting in multiwell plates, Biofabrication 13 (2021) 025007, https://doi.org/10.1088/1758-5090/ab89ca.

[24] J. Liu, J. He, J. Liu, X. Ma, Q. Chen, N. Lawrence, W. Zhu, Y. Xu, S. Chen, Rapid 3D bioprinting of in vitro cardiac tissue models using human embryonic stem cell-derived cardiomyocytes, Bioprinting 13 (2019) e00040, https://doi.org/10.1016/j.bprint.2019.e00040.

[25] C. Yu, J. Schimelman, P. Wang, K.L. Miller, X. Ma, S. You, J. Guan, B. Sun, W. Zhu, S. Chen, Photopolymerizable biomaterials and light-based 3D printing strategies for biomedical applications, Chem. Rev. 120 (2020) 10695–10743, https://doi.org/10.1021/acs.chemrev.9b00810.

[26] C. Yu, K.L. Miller, J. Schimelman, P. Wang, W. Zhu, X. Ma, M. Tang, S. You, D. Lakshmipathy, F. He, S. Chen, A sequential 3D bioprinting and orthogonal bioconjugation approach for precision tissue engineering, Biomaterials 258 (2020) 120294, https://doi.org/10.1016/j.biomaterials.2020.120294.

[27] M. Tang, S.K. Tiwari, K. Agrawal, M. Tan, J. Dang, T. Tam, J. Tian, X. Wan, J. Schimelman, S. You, Q. Xia, T.M. Rana, S. Chen, Rapid 3D bioprinting of glioblastoma model mimicking native biophysical heterogeneity, Small 17 (2021) 2006050, https://doi.org/10.1002/smll.202006050.

[28] J.D. Humphrey, E.R. Dufresne, M.A. Schwartz, Mechanotransduction and extracellular matrix homeostasis, Nat. Rev. Mol. Cell Biol. 15 (2014) 802–812, https://doi.org/10.1038/nrm3896.

[29] D.T. Butcher, T. Alliston, V.M. Weaver, A tense situation: forcing tumour progression, Nat. Rev. Cancer 9 (2009) 108–122, https://doi.org/10.1038/nrc2544.

[30] D. Chauvet, M. Imbault, L. Capelle, C. Demene, M. Mossad, C. Karachi, A.-L. Boch, J.-L. Gennisson, M. Tanter, In vivo measurement of brain tumor elasticity using intraoperative shear wave elastography, Ultraschall der Med. 37 (2016) 584–590, https://doi.org/10.1055/s-0034-1399152.

[31] X. He, Y. Yang, Y. Han, C. Cao, Z. Zhang, L. Li, C. Xiao, H. Guo, L. Wang, L. Han, Z. Qu, N. Liu, S. Han, F. Xu, Extracellular Matrix Physical Properties Govern the Diffusion of Nanoparticles in Tumor Microenvironment, vol. 120, Proceedings of

[32] R.-Z. Tang, X.-Q. Liu, Biophysical cues of in vitro biomaterials-based artificial extracellular matrix guide cancer cell plasticity, Mater Today Bio 19 (2023) 100607, https://doi.org/10.1016/j.mtbio.2023.100607.

[33] A.V. Taubenberger, S. Girardo, N. Träber, E. Fischer-Friedrich, M. Kräter, K. Wagner, T. Kurth, I. Richter, B. Haller, M. Binner, D. Hahn, U. Freudenberg, C. Werner, J. Guck, 3D microenvironment stiffness regulates tumor spheroid growth and mechanics via p21 and ROCK, Adv Biosyst 3 (2019) e1900128, https://doi.org/10.1002/adbi.201900128.

[34] S.A. Richman, S. Nunez-Cruz, B. Moghimi, L.Z. Li, Z.T. Gershenson, Z. Mourelatos, D.M. Barrett, S.A. Grupp, M.C. Milone, High-affinity GD2-specific CAR T cells induce fatal encephalitis in a preclinical neuroblastoma model, Cancer Immunol. Res. 6 (2018) 36–46, https://doi.org/10.1158/2326-6066.CIR-17-0211.

[35] R.G. Majzner, S. Ramakrishna, K.W. Yeom, S. Patel, H. Chinnasamy, L.M. Schultz, R.M. Richards, I. Jiang, V. Barsan, R. Mancusi, A.C. Geraghty, Z. Good, A. Y. Mochizuki, S.M. Gillespie, A.M.S. Toland, J. Mahdi, A. Reschke, E.H. Nie, I. J. Chau, M.C. Rotiroti, C.W. Mount, C. Baggott, S. Mavroukakis, E. Egeler, J. Moon, C. Erickson, S. Green, M. Kunicki, M. Fujimoto, Z. Ehlinger, W. Reynolds, S. Kurra, K.E. Warren, S. Prabhu, H. Vogel, L. Rasmussen, T.T. Cornell, S. Partap, P.G. Fisher, C.J. Campen, M.G. Filbin, G. Grant, B. Sahaf, K.L. Davis, S.A. Feldman, C. L. Mackall, M. Monje, GD2-CAR T cell therapy for H3K27M-mutated diffuse midline gliomas, Nature 603 (2022) 934–941, https://doi.org/10.1038/s41586-022-04489-4.

[36] G. Golinelli, G. Grisendi, M. Prapa, M. Bestagno, C. Spano, F. Rossignoli, F. Bambi, I. Sardi, M. Cellini, E.M. Horwitz, A. Feletti, G. Pavesi, M. Dominici, Targeting GD2-positive glioblastoma by chimeric antigen receptor empowered mesenchymal progenitors, Cancer Gene Ther. 27 (2020) 558–570, https://doi.org/10.1038/s41417-018-0062-x.

[37] S. Rafiq, C.S. Hackett, R.J. Brentjens, Engineering strategies to overcome the current roadblocks in CAR T cell therapy, Nat. Rev. Clin. Oncol. 17 (2020) 147–167, https://doi.org/10.1038/s41571-019-0297-y.

[38] C. Lin, Y. Zhang, K. Zhang, Y. Zheng, L. Lu, H. Chang, H. Yang, Y. Yang, Y. Wan, S. Wang, M. Yuan, Z. Yan, R. Zhang, Y. He, G. Ge, D. Wu, J. Chen, Fever promotes T lymphocyte trafficking via a thermal sensory pathway involving heat shock protein 90 and α4 integrins, Immunity 50 (2019) 137–151.e6, https://doi.org/10.1016/j.immuni.2018.11.013.

[39] S.S. Evans, E.A. Repasky, D.T. Fisher, Fever and the thermal regulation of immunity: the immune system feels the heat, Nat. Rev. Immunol. 15 (2015) 335–349, https://doi.org/10.1038/nri3843.

[40] Y. Kobayashi, Y. Ito, M. Sakai, M. Matsushita, K. Imai, K. Shimizu, A. Aruga, K. Tanigawa, Whole-body heat treatment stimulates antigen-specific T cell responses in human system, Journal for ImmunoTherapy of Cancer 1 (2013) P131, https://doi.org/10.1186/2051-1426-1-S1-P131.

[41] D. O'Sullivan, M.A. Stanczak, M. Villa, F.M. Uhl, M. Corrado, R.I. Klein Geltink, D. E. Sanin, P. Apostolova, N. Rana, J. Edwards-Hicks, K.M. Grzes, A.M. Kabat, R. L. Kyle, M. Fabri, J.D. Curtis, M.D. Buck, A.E. Patterson, A. Regina, C.S. Field, F. Baixauli, D.J. Puleston, E.J. Pearce, R. Zeiser, E.L. Pearce, Fever supports CD8+ effector T cell responses by promoting mitochondrial translation, Proc. Natl. Acad. Sci. U. S. A. 118 (2021) e2023752118, https://doi.org/10.1073/pnas.2023752118.

[42] Y. Wu, Y. Liu, Z. Huang, X. Wang, Z. Jin, J. Li, P. Limsakul, L. Zhu, M. Allen, Y. Pan, R. Bussell, A. Jacobson, T. Liu, S. Chien, Y. Wang, Control of the activity of CAR-T cells within tumours via focused ultrasound, Nat. Biomed. Eng. 5 (2021) 1336–1347, https://doi.org/10.1038/s41551-021-00779-w.

[43] N. Colwell, M. Larion, A.J. Giles, A.N. Seldomridge, S. Sizdahkhani, M.R. Gilbert, D.M. Park, Hypoxia in the glioblastoma microenvironment: shaping the phenotype of cancer stem-like cells, Neuro Oncol. 19 (2017) 887–896, https://doi.org/10.1093/neuonc/now258.

[44] D. Gumber, L.D. Wang, Improving CAR-T immunotherapy: overcoming the challenges of T cell exhaustion, EBioMedicine 77 (2022), https://doi.org/10.1016/j.ebiom.2022.103941.

[45] I.C. Miller, A. Zamat, L.-K. Sun, H. Phuengkham, A.M. Harris, L. Gamboa, J. Yang, J.P. Murad, S.J. Priceman, G.A. Kwong, Enhanced intratumoural activity of CAR T cells engineered to produce immunomodulators under photothermal control, Nat. Biomed. Eng. 5 (2021) 1348–1359, https://doi.org/10.1038/s41551-021-00781-2.

[46] E.W. Weber, K.R. Parker, E. Sotillo, R.C. Lynn, H. Anbunathan, J. Lattin, Z. Good, J. A. Belk, B. Daniel, D. Klysz, M. Malipatlolla, P. Xu, M. Bashti, S. Heitzeneder, L. Labanieh, P. Vandris, R.G. Majzner, Y. Qi, K. Sandor, L.-C. Chen, S. Prabhu, A. J. Gentles, T.J. Wandless, A.T. Satpathy, H.Y. Chang, C.L. Mackall, Transient rest restores functionality in exhausted CAR-T cells through epigenetic remodeling, Science 372 (2021) eaba1786, https://doi.org/10.1126/science.aba1786.

[47] M.L. Davila, I. Riviere, X. Wang, S. Bartido, J. Park, K. Curran, S.S. Chung, J. Stefanski, O. Borquez-Ojeda, M. Olszewska, J. Qu, T. Wasielewska, Q. He, M. Fink, H. Shinglot, M. Youssif, M. Satter, Y. Wang, J. Hosey, H. Quintanilla, E. Halton, Y. Bernal, D.C.G. Bouhassira, M.E. Arcila, M. Gonen, G.J. Roboz, P. Maslak, D. Douer, M.G. Frattini, S. Giralt, M. Sadelain, R. Brentjens, Efficacy and toxicity management of 19-28z CAR T cell therapy in B cell acute lymphoblastic leukemia, Sci. Transl. Med. 6 (2014), https://doi.org/10.1126/scitranslmed.3008226, 224ra25.

[48] R.A. Morgan, J.C. Yang, M. Kitano, M.E. Dudley, C.M. Laurencot, S.A. Rosenberg, Case report of a serious adverse event following the administration of T cells transduced with a chimeric antigen receptor recognizing ERBB2, Mol. Ther. 18 (2010) 843–851, https://doi.org/10.1038/mt.2010.24.

[49] Y. Pan, S. Yoon, J. Sun, Z. Huang, C. Lee, M. Allen, Y. Wu, Y.-J. Chang, M. Sadelain, K.K. Shung, S. Chien, Y. Wang, Mechanogenetics for the remote and noninvasive

control of cancer immunotherapy, Proc. Natl. Acad. Sci. USA 115 (2018) 992–997, https://doi.org/10.1073/pnas.1714900115.